




Magnetism in the $S = 1$ triangular dimer lattice antiferromagnet $\text{K}_2\text{Ni}_2(\text{SeO}_3)_3$

Z. R. Li, Z. W. Ouyang ^{*}, J. J. Cao, L. Wang, Z. X. Wang, Z. C. Xia , and J. F. Wang
*Wuhan National High Magnetic Field Center & School of Physics,
 Huazhong University of Science and Technology, Wuhan 430074, People's Republic of China*

 (Received 10 May 2023; revised 5 April 2024; accepted 22 May 2024; published 10 June 2024)

We report an $S = 1$ antiferromagnet $\text{K}_2\text{Ni}_2(\text{SeO}_3)_3$ crystalizing in the hexagonal space group $P6_3/mmc$. The structure consists of the perpendicular-to-plane Ni_2O_9 dimers in the triangular layers. Surprisingly, $\text{K}_2\text{Ni}_2(\text{SeO}_3)_3$ exhibits a sharp upturn of magnetic susceptibility below $T_N = 5.8$ K, a single or two-step antiferromagnetic transitions at T_{N1} and T_{N2} , whose values are magnetic-field dependent, and a sign of $1/3$ -like magnetization plateau at 2 K, all of which are typical features for a triangular-lattice antiferromagnet with small easy-axis anisotropy rather than the $S = 1$ dimer compound. The density functional theory calculations prove the small intradimer exchange ($J_0/k_B = -2.11$ K) and the large intraplane interdimer exchanges ($J_1/k_B = -13.27$ K); the latter originates from the two Ni-O-Se-O-Ni super-superexchange paths within the triangular plane. This feature makes $\text{K}_2\text{Ni}_2(\text{SeO}_3)_3$ a triangular-lattice antiferromagnet with small easy-axis anisotropy, rather than a spin-dimer antiferromagnet.

DOI: [10.1103/PhysRevB.109.224413](https://doi.org/10.1103/PhysRevB.109.224413)

I. INTRODUCTION

Topological structure plays a crucial role in the magnetism of quantum magnets. In a pure two-dimensional (2D) triangular-lattice antiferromagnet (TLAF), classical 120° spin order, $1/3$ magnetization plateau, and possible spin-liquid state were often reported (see Refs. [1,2] and references therein). On the other hand, an interacting dimer antiferromagnetic (AFM) system has been regarded to be a typical platform for investigating the coexistence of classical and quantum magnetism and the so-called “quantum criticality” [3–7]. Different from the well-understood pure $S = 1/2$ dimer—a sharp quantum phase transition can be driven by a critical magnetic field $H_c = \Delta/g\mu_B$, where Δ is the spin gap between the singlet state and the $S_z = 1$ -triplet state [8], the interdimer interactions in the interacting dimer system decrease the size of spin gap, bringing about quantum criticality and exotic magnetic properties such as magnetization plateaus and Bose-Einstein condensation [3,7], particle-hole symmetry breaking [9], supersolid state and incomplete devil’s staircase [10,11], and the amplitude (Higgs) excitation mode [4–6,12].

Topologically, dimers can form chains like in $\text{BaCo}_2(\text{SeO}_3)_3 \cdot 3\text{H}_2\text{O}$ [13] and ACuCl_3 ($A = \text{K, Tl, NH}_4$) [3,5,9,12,14–16], 2D square lattice like in Han purple pigment $\text{BaCuSi}_2\text{O}_6$ [4,6,17], orthogonal Shastry-Sutherland lattice as realized in $\text{SrCu}(\text{BO}_3)_2$ [10,11,18], etc. Of the particularly interesting are triangular-dimer systems such as $\text{Cs}_3\text{M}_2\text{X}_9$ ($M = \text{Cr, Fe; X} = \text{Br, Cl}$) [19,20] and $\text{A}_3\text{M}_2\text{O}_8$ ($A = \text{Ba, Sr; M} = \text{Cr, Mn}$) [21–27], in which a combination of single-state dimer and geometric frustrated triangular lattice produces a great wealth of unexpected quantum phenomena and effects like multiple

field-induced phases [20], field-induced triplet (quintuplet) condensates [23,24], spin density wave and spiral phases [25], orbital-lattice fluctuations [26], and magnonic liquid phase [27]. Therefore, it is of particular interest to investigate the triangular-dimer-lattice compounds.

Here, we successively synthesized an $S = 1$ antiferromagnet $\text{K}_2\text{Ni}_2(\text{SeO}_3)_3$ and its structure and magnetism are investigated. The compound crystallizes in the hexagonal structure (space group $P6_3/mmc$) with the Ni_2O_9 dimers forming a 2D triangular lattice. The magnetic susceptibility exhibits a sharp upturn below $T_N = 5.8$ K. The specific heat data show that $\text{K}_2\text{Ni}_2(\text{SeO}_3)_3$ undergoes a single or two-step AFM transitions at T_{N1} and T_{N2} , whose values are field dependent. The high-field magnetization curve at 2 K for the c axis presents a sign of $1/3$ -like magnetization plateau. These features quite resemble those of the TLAFs with small easy-axis anisotropy, rather than the spin-dimer antiferromagnets. Also, the magnetism of $\text{K}_2\text{Ni}_2(\text{SeO}_3)_3$ is quite different from those of triangular-dimer compounds mentioned above and the isomorphic $S_{\text{eff}} = 1/2$ Co compound $\text{K}_2\text{Co}_2(\text{SeO}_3)_3$ [28,29]. The $\text{K}_2\text{Co}_2(\text{SeO}_3)_3$ is not magnetically ordered down to 0.35 K, exhibits the feature of the Co dimer, and presents a well-defined unexplained magnetization plateau. The theoretical calculations are utilized to interpret the experimental results of $\text{K}_2\text{Ni}_2(\text{SeO}_3)_3$.

II. EXPERIMENTAL AND COMPUTATIONAL DETAILS

Single crystals of $\text{K}_2\text{Ni}_2(\text{SeO}_3)_3$ were synthesized by solid-state reaction at high temperature. Stoichiometric amounts of K_2CO_3 (99.99%), NiO (99.99%), and SeO_2 (99.99%) were mixed and loaded in an alumina crucible. The mixture was sealed in an evacuated quartz tube and heated at 900°C for 600 min and then cooled down to room temperature at a speed of 3°C/h . Yellow single crystals with

*zwouyang@mail.hust.edu.cn

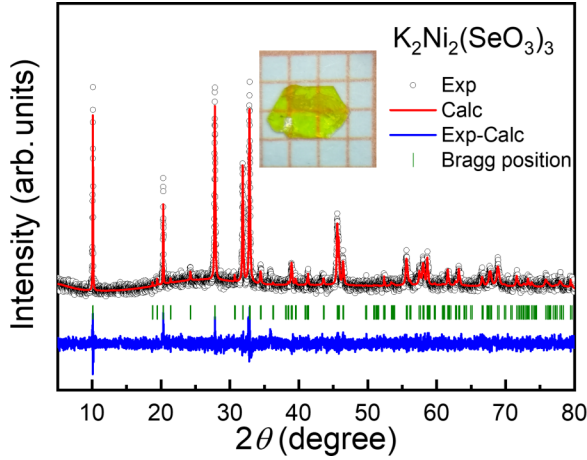


FIG. 1. Experimental and calculated XRD patterns as well as their difference for the powder sample of $\text{K}_2\text{Ni}_2(\text{SeO}_3)_3$. The green vertical bars are the expected Bragg reflections. The inset: a photo of the single crystal with a size of $2 \times 3 \times 0.3 \text{ mm}^3$.

typical size of $2 \times 3 \times 0.3 \text{ mm}^3$ were obtained (see the inset of Fig. 1). With the SHELXTL software [30], the crystal structure was solved by analyzing single-crystal x-ray diffraction (XRD) data collected at 293 K on an Oxford Diffraction Xcalibur3 CCD diffractometer with graphite-monochromated Mo $K\alpha$ radiation ($\lambda = 0.71073 \text{ \AA}$). The powder XRD data of the crushed crystals used for structure refinement were collected on a PANalytical X'Pert powder XRD with Cu $K\alpha$ radiation. The magnetization/magnetic susceptibility and specific heat were measured by a superconducting quantum interference device (SQUID) magnetometer and a physical properties measurement system (PPMS), respectively. The high-field magnetization measurements were carried out in pulsed magnetic fields up to 50 T by an inductive technique.

Theoretical calculations were carried out based on first-principles density functional theory (DFT) using standard generalized gradient approximations (GGA) with the Perdew-Burke-Ernzerhof parametrization for the exchange correlation [31]. To include the $3d$ -electron correlations, we used the GGA+ U scheme with effective $U_{\text{eff}} = U - J = 0, 4$ and 6 eV , where U and J are on-site Coulomb and exchange interactions, respectively. We used the accurate full-potential linearized augmented plane wave method as implemented in the WIEN2K package [32]. The refined crystal structure data were used in the calculations. A mesh of 100 k points was employed in the Brillouin zone. The convergence criterion for the total energy was 10^{-5} Ry . The exchange interactions were calculated using the following Heisenberg model:

$$H = - \sum_{ij} J_{ij} S_i \cdot S_j, \quad (1)$$

where J_{ij} is the exchange parameter between two spin sites (i, j) and the summation runs over each pair. The value of J_{ij} can be determined by comparing the total energies of different spin configurations. Only collinear spin configurations are considered in the calculations.

TABLE I. Crystallographic data and structural refinements for $\text{K}_2\text{Ni}_2(\text{SeO}_3)_3$.

Formula	$\text{K}_2\text{Ni}_2(\text{SeO}_3)_3$
Formula weight	566.50
T (K)	293(2)
Space group	$P6_3/mmc$
λ (\AA)	0.71073
a (\AA)	5.4506(2)
b (\AA)	5.4506(2)
c (\AA)	17.4695(9)
α (deg)	90
β (deg)	90
γ (deg)	120
Volume (\AA^3)	449.46(5)
Z	2
Density (g/cm^3)	4.260
GOF	1.103
$R_1, wR_2 [I > 2\sigma(I)]^a$	0.0277, 0.0731
R_1, wR_2 (all data)	0.0340, 0.0758

$$^a R_1 = \sum ||F_o| - |F_c||;$$

$$wR_2 = \{\sum w[(F_o)^2 - (F_c)^2]^2 / \sum w[(F_o)^2]^2\}^{1/2}$$

III. RESULTS AND DISCUSSION

A. Structure and magnetic properties

The single crystal XRD analysis reveals that the synthesized crystals of $\text{K}_2\text{Ni}_2(\text{SeO}_3)_3$ are single phase with hexagonal structure (space group $P6_3/mmc$, No. 194), isostructural to $\text{K}_2\text{Co}_2(\text{SeO}_3)_3$ [28,29]. The lattice parameters are $a = b = 5.4506(2) \text{ \AA}$, $c = 17.4695(9) \text{ \AA}$, $\alpha = \beta = 90^\circ$, and $\gamma = 120^\circ$. The detailed crystallographic data and atomic positions are listed in Tables I and II. As shown in Fig. 1, the difference between the experimental and calculated XRD patterns for the powder sample indicates the sample is of high quality and there is no secondary phase.

The crystal structure of $\text{K}_2\text{Ni}_2(\text{SeO}_3)_3$ is shown in Figs. 2(a) and 2(b). All positions are completely occupied except for the Se2 atom which splits into two sites and each is half occupied. There is only one independent crystallographic site of the Ni^{2+} ion coordinated by six nearest oxygen atoms. The NiO_6 octahedron is significantly stretched along the c axis, as can be seen from the O-Ni-O angles [see Fig. 2(a)]. The NiO_6 octahedra are face shared to form the Ni_2O_9 dimer along the c axis with a Ni-Ni bond length of $d_0 = 2.9116(18) \text{ \AA}$. Each unit cell contains two Ni_2O_9 dimers.

TABLE II. Wyckoff positions, coordinates, occupancies, and equivalent isotropic displacement parameters, respectively, for $\text{K}_2\text{Ni}_2(\text{SeO}_3)_3$.

Atom	Wyckoff site	x	y	z	S.O.F	U_{eq}
Ni	4f	1.33333	0.66667	0.33333	1	0.010
Se1	4e	1.00000	0.00000	0.35856	1	0.008
Se2	4f	0.666667	0.333333	0.21473	0.5	0.007
K	4f	1.33333	0.66667	0.53501	1	0.023
O1	12k	1.16030	0.32070	0.40250	1	0.014
O2	6h	0.99700	0.49850	0.25000	1	0.014

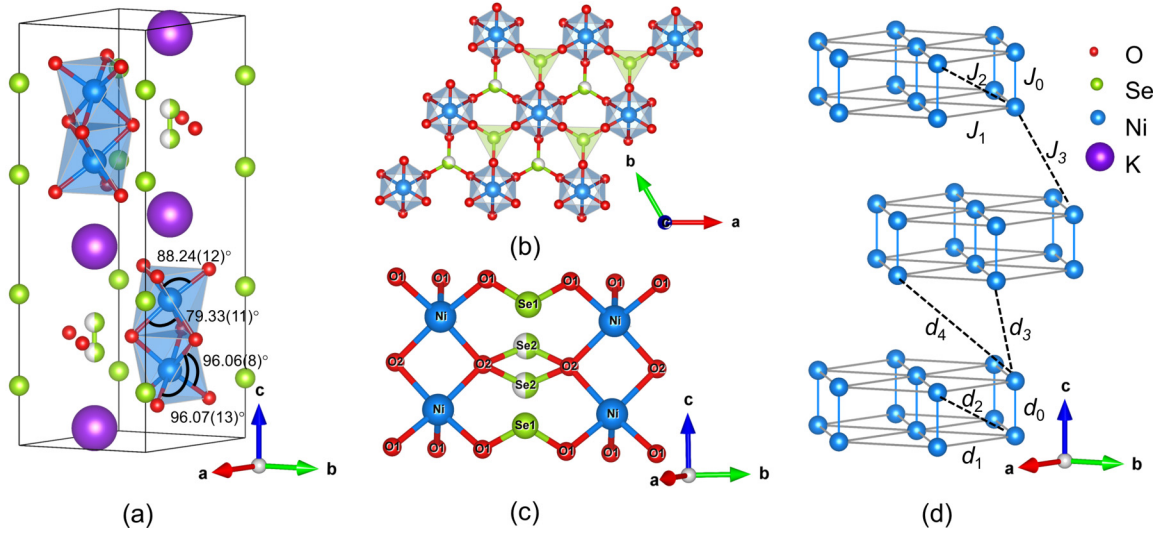


FIG. 2. Crystal structure of $\text{K}_2\text{Ni}_2(\text{SeO}_3)_3$. (a) The unit cell and the Ni_2O_9 dimer with the O-Ni-O angles. (b) The basal ab plane showing the triangular magnetic lattice. (c) Two SSE paths (Ni-O1-Se1-O1-Ni and Ni-O2-Se2-O2-Ni) for J_1 and one SSE path (Ni-O2-Se2-O2-Ni) for J_2 , where Se2 is half occupied. (d) Topological arrangement of the Ni^{2+} ions. The intradimer Ni-Ni distance $d_0 = 2.9116(18)$ Å (J_0), the intraplane Ni-Ni distances between the adjacent dimers $d_1 = 5.4506(3)$ Å (J_1) and $d_2 = 6.1795(9)$ Å (J_2), and the interlayer nearest and the next nearest neighbor Ni-Ni distances $d_3 = 6.6191(16)$ Å (J_3) and $d_4 = 8.5745(13)$ Å.

Interestingly, the perpendicular-to-plane Ni_2O_9 dimers are bridged by the tripodlike $(\text{Se}_2\text{O}_3)^{2-}$ group, forming an equilateral triangular lattice in the ab plane [Fig. 2(b)]. The Ni-Ni distances of the intraplane adjacent dimers are $d_1 = 5.4506(3)$ Å and $d_2 = 6.1795(9)$ Å. The dimer triangular layers are stacked in an A - B - A - B mode along the c axis and separated by nonmagnetic K^+ ions. Thus good two dimensionality is expected. The nearest and the next nearest neighbor Ni-Ni distances between the adjacent triangular layers are $d_3 = 6.6191(16)$ Å and $d_4 = 8.5745(13)$ Å, respectively. Topological structure of the magnetic Ni^{2+} ions is schematically shown in Fig. 2(d), which is quite similar to the triangular-dimer compounds $\text{A}_3\text{M}_2\text{O}_8$ [21,22]. In Fig. 3(a) we show the magnetic susceptibility $\chi(T)$ and the inverse $1/\chi(T)$ curves of $\text{K}_2\text{Ni}_2(\text{SeO}_3)_3$ measured at 0.1 T. Here, only the zero-field-cooled heating curves are shown because no heat hysteresis is observed. At high temperatures, the $\chi(T)$ curve complies with the modified Curie-Weiss law $\chi(T) = \chi_0 + \frac{C}{(T - \theta_{\text{CW}})}$, where χ_0 is the temperature-independent term, C is the Curie constant, and θ_{CW} is the Curie-Weiss temperature. The fit of the $1/\chi(T)$ curve within 100–300 K gives $\theta_{\text{CW}} = -52.77$ K and the effective magnetic moment $\mu_{\text{eff}} = 3.13\mu_{\text{B}}/\text{Ni}$ ($g_{ab} = 2.21$) when the magnetic field is applied along the ab plane ($H \parallel ab$) and $\theta_{\text{CW}} = -48.52$ K and $\mu_{\text{eff}} = 3.30\mu_{\text{B}}/\text{Ni}$ ($g_c = 2.33$) when the magnetic field is applied along the c axis ($H \parallel c$). The values of μ_{eff} are larger than theoretical value of $2.83\mu_{\text{B}}/\text{Ni}$ ($S = 1$ and $g = 2$) due to the orbital moment contribution of the Ni^{2+} ion. The large negative θ_{CW} shows the predominant AFM interaction in $\text{K}_2\text{Ni}_2(\text{SeO}_3)_3$ and the small difference of θ_{CW} between $H \parallel c$ and $H \parallel ab$ reflects the presence of small magnetic anisotropy.

Figure 3(a) also reveals that at low temperatures the $\chi(T)$ curve for $H \parallel c$ deviates upward from the curve for $H \parallel ab$, indicative of the axial anisotropy. Note that no broad maximum expected for a spin-dimer antiferromagnet is observed.

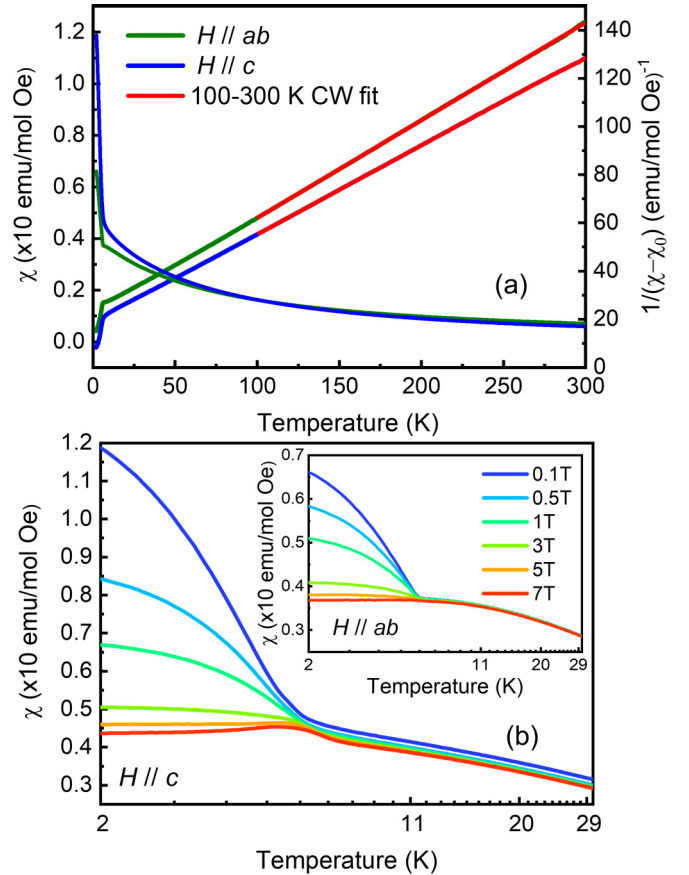


FIG. 3. (a) $\chi(T)$ curves of the $\text{K}_2\text{Ni}_2(\text{SeO}_3)_3$ single crystal measured at 0.1 T. The red solid lines are Curie-Weiss fits from 100 to 300 K. (b) The $\chi(T)$ curves from 2 to 30 K measured at different magnetic fields.

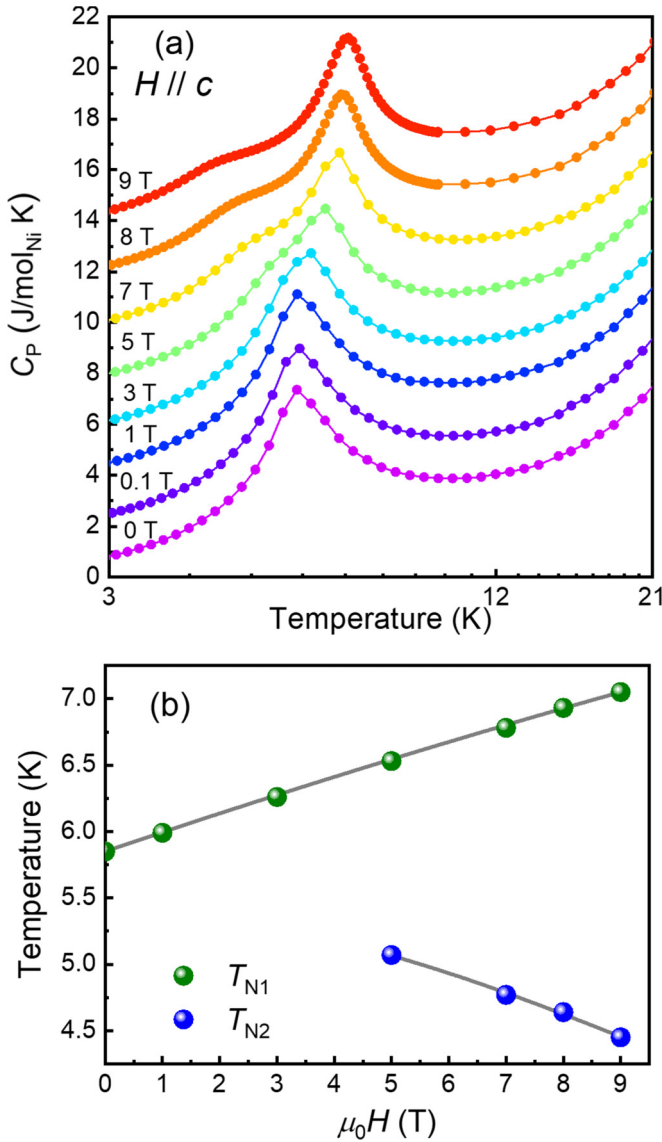


FIG. 4. (a) Specific heat C_p measured at different magnetic fields for $H \parallel c$. The curves are shifted up by different magnitudes in relation to the zero-field curve. (b) The field dependencies of T_{N1} and T_{N2} for $H \parallel c$.

Instead, a sharp upturn of susceptibility is seen at $T_N = 5.8$ K due to the long-range AFM order. Such a sharp upturn is quite similar to that observed in the $S = 1$ TLAF $\text{Ba}_2\text{La}_2\text{NiTe}_2\text{O}_{12}$ [33] with small easy-axis anisotropy and interlayer ferromagnetic (FM) exchange. Assuming there are sizable intraplane exchanges, geometric frustration is expected. The frustrated factor, which is defined as $f = |\theta_{\text{CW}}|/T_N$, is about 10 for $H \parallel ab$, implying a strong magnetic frustration within the ab plane. It is worth noting that the sharp upturn of the $\chi(T)$ curve is gradually suppressed with increasing magnetic field [see Fig. 3(b)]. The $\chi(T)$ curve for $H \parallel c$ presents a rounded peak, which is particularly pronounced for the 7 T data. This might imply the presence of two magnetic phase transitions.

Therefore, we measured the specific heat $C_p(T)$ for $H \parallel c$ as shown in [Fig. 4(a)]. In the zero-field $C_p(T)$ curve,

the λ -like peak evidences the long-range AFM ordering at $T_N = 5.8$ K. When the magnetic field increases, the $C_p(T)$ curve is gradually broadened. At 5 T, the curve consists of a strong peak at $T_{N1} = 6.5$ K and a weak peak at $T_{N2} = 5.1$ K, showing the presence of two magnetic phase transitions. Further increasing the field, the two peaks separate from each other. The strong peak at T_{N1} moves towards high temperature without significant change in intensity, while the weak peak at T_{N2} shifts to low temperature with a decrease in intensity. As shown in Fig. 4(b), both T_{N1} and T_{N2} vary nonlinearly with magnetic field.

Theory predicted that two-step magnetic transitions occur in TLAFs with an easy-axis type of anisotropy, while a single transition is expected for easy-plane anisotropy [34]. In the two-step transitions, the c -axis component of spins orders first at T_{N1} and then the ab components order at T_{N2} . According to this scenario, $\text{K}_2\text{Ni}_2(\text{SeO}_3)_3$ with single-step transition at zero field should be of easy-plane anisotropy, which conflicts with the observed easy-axis-type anisotropy [Fig. 3(a)]. This might be understood as follows. On the one hand, a scrutiny of Fig. 4(a) reveals that the zero-field $C_p(T)$ curve exhibits only a less sharp peak and the evolution of $C_p(T)$ with the magnetic field is a gradual process without a sudden change in peak width. Hence the presence of two-step transitions in the $C_p(T)$ curve below 5 T cannot be ruled out completely. On the other hand, if there is really only one peak in the $C_p(T)$ curve, it is also not surprising; after all, the $\text{K}_2\text{Ni}_2(\text{SeO}_3)_3$ is not a standard TLAF and it contains a dimer structure. In the isomorphous $S_{\text{eff}} = 1/2$ Co compound $\text{K}_2\text{Co}_2(\text{SeO}_3)_3$ with easy-axis anisotropy, zero-field $C_p(T)$ curve presents a broad peak around 5 K [29]. Even in a usual TLAF with easy-axis anisotropy, a single-step transition in the $C_p(T)$ curve can also be observed and a recent example is the $S_{\text{eff}} = 1/2$ compound $\text{A}_2\text{Co}_2(\text{SeO}_3)_3$ ($A = \text{K}, \text{Rb}$) [35]. In addition, in $\text{A}_3\text{NiNb}_2\text{O}_9$ ($A = \text{Sr}, \text{Ca}$) [36,37] with distorted structure, two magnetic transitions are observed but the expected easy-axis anisotropy was excluded by the inelastic neutron scattering measurements. Therefore, the scenario above seems to be not an iron rule.

Furthermore, in some TLAFs like $\text{Ba}_3\text{CoT}_2\text{O}_9$ ($T = \text{Nb}, \text{Ta}$) with $S_{\text{eff}} = 1/2$ [38,39], $\text{A}_3\text{NiT}_2\text{O}_9$ ($A = \text{Ba}, \text{Sr}, \text{Ca}; T = \text{Nb}, \text{Ta}$) with $S = 1$ [36,37,40,41], and $\text{Li}_2\text{Co}(\text{WO}_4)_2$ with $S = 3/2$ [42], the T_{N1} and T_{N2} move to lower temperature as magnetic field increases. However, in $\text{A}_2\text{Co}(\text{SeO}_3)_2$ ($A = \text{K}, \text{Rb}$) with $S_{\text{eff}} = 1/2$ [35] and $\text{Ba}_2\text{La}_2\text{NiTe}_2\text{O}_{12}$ with $S = 1$ [33], an increasing field shifts the single or two-step transitions to higher temperature. It is difficult to say whether the magnetic field enhances or weakens the antiferromagnetism of these compounds. The single or two-step transitions as well as their evolution with magnetic field in TLAFs are complex, depending on spin number, lattice geometry, magnetic/spatial anisotropy, and interlayer exchange interaction.

Figure 5(a) shows the pulsed high-field magnetization $M(H)$ curves at 2 K calibrated by the SQUID data for $\text{K}_2\text{Ni}_2(\text{SeO}_3)_3$. When $H \parallel ab$, the magnetization increases nearly linearly due to the AFM character but does not reach magnetic saturation at 50 T due to large AFM interaction. The $M(H)$ curve for $H \parallel c$ is located above the curve for $H \parallel ab$, again showing the small easy-axis anisotropy. The magnetization increases with a small curvature in the low

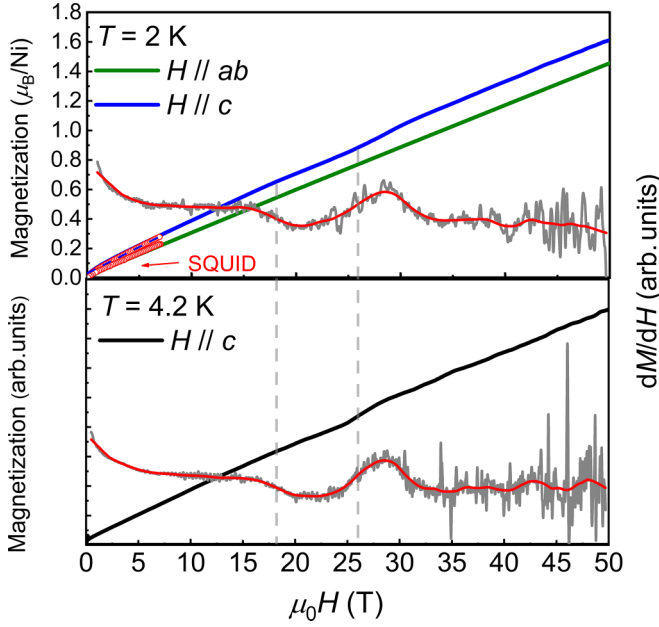


FIG. 5. (a) Pulsed high-field $M(H)$ curves at 2 K calibrated with the SQUID data. The blue dashed line is the extrapolation of the low-field SQUID data for $H \parallel c$. (b) The pulsed high-field $M(H)$ curve at 4.2 K. At both temperatures, the dM/dH curve for $H \parallel c$ is also shown for determining the edge fields H_{c1} and H_{c2} defined as the inflection points of the dM/dH curve (gray lines). The red lines are guides to eyes.

fields, as can be seen from the SQUID data. A zero-field extrapolation of the low-field curve yields $\Delta M = 0.03\mu_B/\text{Ni}$ [see Fig. 5(a)]. Regardless of single or two-step transitions, $\text{K}_2\text{Ni}_2(\text{SeO}_3)_3$ is of easy-axis anisotropy. The ground-state spin configuration is a distorted 120° structure in a plane including the c axis. The zero-field magnetization along the c axis can be expressed as $\Delta M = \frac{1}{3}(2 \cos \theta - 1)g\mu_B S$, where θ is the canting angle between the sublattice spins and the c axis [33]. With $\Delta M = 0.03\mu_B/\text{Ni}$, we have $\theta = 58.45^\circ$ ($g_c = 2.33$). Assume that the single-ion anisotropy D is the origin of the small easy-axis anisotropy; using $\cos \theta = \frac{3J}{6J - 2|D|}$, we have $|D|/J = 0.13$, close to that of $\text{Ba}_2\text{La}_2\text{NiTe}_2\text{O}_{12}$ [33]. Although the obtained D value may not be accurate, it qualitatively confirms the small magnetic anisotropy. Hence the single-ion anisotropy is ignored in the estimation of the above frustrated factor and the following DFT calculations.

Further increasing the magnetic field, a small transition appears in the $M(H)$ curve for $H \parallel c$. This can be conveniently distinguished from the dM/dH curve shown in Fig. 5(a). The lower and higher edge fields, which are defined as the magnetic fields at which dM/dH has inflection points [33], are determined to be $\mu_0 H_{c1} = 18.3$ T and $\mu_0 H_{c2} = 26.2$ T. The averaged magnetization between H_{c1} and H_{c2} is about $0.78\mu_B/\text{Ni}$, close to $1/3$ of the saturated moment $2.33\mu_B/\text{Ni}$ ($g_c = 2.33$). This is a sign of $1/3$ magnetization plateau as often observed in TLAFs with easy-axis anisotropy [33]. The values of H_{c1} and H_{c2} as well as the field range for the $1/3$ -like plateau are approximately one-half of those ($\mu_0 H_{c1} = 32$ T and $\mu_0 H_{c2} = 47$ T) of $\text{Ba}_2\text{La}_2\text{NiTe}_2\text{O}_{12}$ [33]. The synergy

TABLE III. Bond lengths (\AA) and exchange interactions (K) for different U_{eff} (eV).

	$d_{\text{Ni-Ni}}$	$J(\text{DFT}+U)$			
		$U_{\text{eff}} = 0$	4 eV	6 eV	8 eV
J_0/k_B	2.9116(18)	-19.42	-3.80	-2.11	-0.86
J_1/k_B	5.4506(3)	-58.58	-20.95	-13.27	-8.64
J_2/k_B	6.1795(9)	-1.10	-0.21	-0.06	-0.07
J_3/k_B	6.6191(16)	-0.97	-0.34	-0.18	-0.10
θ_{CW}		-253.61	-87.85	-55.09	-35.61

between the easy-axis anisotropy and the quantum fluctuations stabilizes the $1/3$ magnetization plateau for $H \parallel c$, but when $H \parallel c$ the easy-axis anisotropy acts to suppress the plateau width. In Fig. 5(b), the $M(H)$ curve obtained at 4.2 K as well as its dM/dH curve are also presented to demonstrate the reproducibility of the small transition. Clearly, no $1/2$ magnetization plateau expected for an $S = 1$ spin-dimer antiferromagnet appears.

The sharp upturn of susceptibility below T_N , the single or two-step magnetic transitions at T_{N1} and T_{N2} in the $C_p(T)$ curve, and the sign of the $1/3$ -like magnetization plateau in the $M(H)$ curve are reminiscent of the magnetic properties of TLAFs rather than those of spin dimer antiferromagnets. This is confusing and significantly contrary to intuition, since the intradimer Ni-Ni distance [2.9116(18) \AA] is much smaller than the intraplane Ni-Ni distances [5.4506(3) \AA and 6.1795(9) \AA]. We therefore postulate that there exists large intraplane AFM exchange that drives $\text{K}_2\text{Ni}_2(\text{SeO}_3)_3$ to become a strongly frustrated TLAF. This is evidenced by the following DFT calculations.

B. DFT calculations

As shown in Fig. 6(a), our calculations adopt a supercell of $2 \times 2 \times 1$ that contains four types of exchanges: intradimer J_0 , intraplane interdimer J_1 and J_2 , and interplane J_3 . We calculate the total energy of one FM and four AFM spin configurations. The results show that the AFM-2 state is the most stable in energy. The exchange parameters are obtained by mapping the total energies of the five spin configurations onto the Heisenberg Hamiltonian equation (1). The Curie-Weiss temperature is estimated with $\theta_{\text{CW}} = \sum_i S(S+1)z_i J_i / 3k_B$, where z_i is the number of nearest-neighbor spins for the exchange J_i and k_B is the Boltzmann constant. The exchange parameters and the value of θ_{CW} for each U_{eff} are listed in Table III. For $U_{\text{eff}} = 6$ eV, we have $J_0/k_B = -2.11$ K, $J_1/k_B = -13.27$ K, $J_2/k_B = -0.06$ K, $J_3/k_B = -0.18$ K, and $\theta_{\text{CW}} = -55.09$ K. The value of θ_{CW} is close to the experimental values (-52.77 K for $H \parallel ab$ and -48.52 K for $H \parallel c$). The dominant J_1 in $\text{K}_2\text{Ni}_2(\text{SeO}_3)_3$ is almost one-half of that ($J_1/k_B = -25$ K) in $\text{Ba}_2\text{La}_2\text{NiTe}_2\text{O}_{12}$, which is in line with the fact that θ_{CW} in the former is approximately one-half of that ($\theta_{\text{CW}} = -100.7$ K) in the latter [33]. Based on $g\mu_B H_s = 9J_1 S$ [33], the saturation field is estimated as $g\mu_B H_s = 80.9$ T, which is much larger than the experimental field of 50 T. All these show that the calculated exchange parameters are reasonable. The very small interplane J_3 reflects

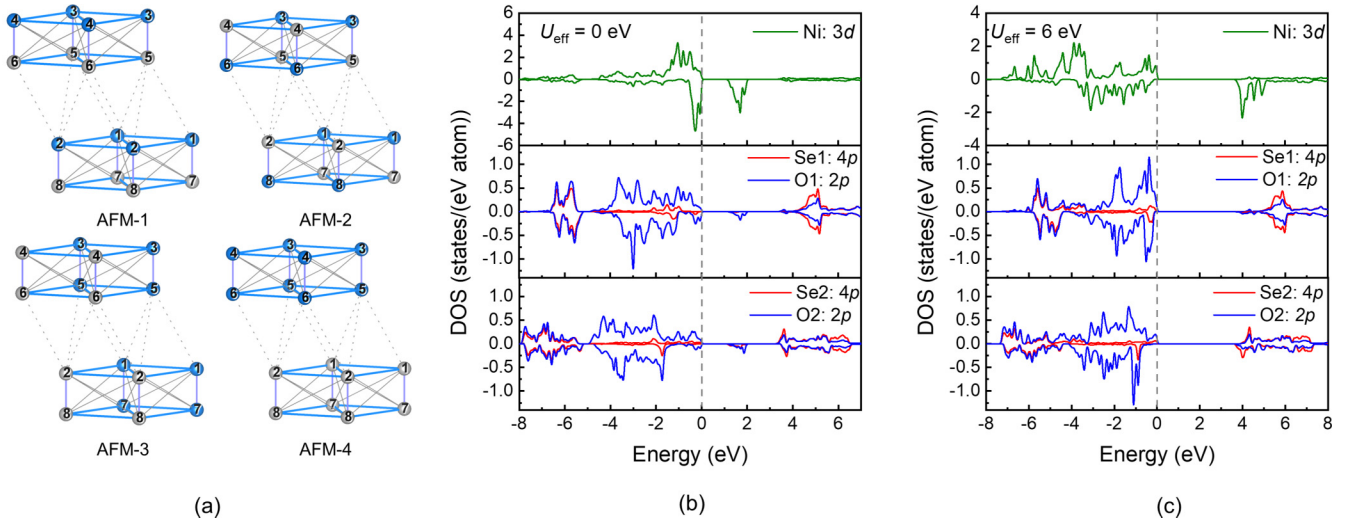


FIG. 6. (a) $2 \times 2 \times 1$ supercell adopted in the DFT calculations. There are eight Ni^{2+} ions labeled with 1–8. The gray and blue spheres correspond to up and down spins on the Ni^{2+} ions. (b),(c) The partial densities of states (DOS) of the Ni $3d$, O $2p$, and Se $4p$ orbitals associated with J_0 , J_1 , and J_2 for the calculated ground state.

good two dimensionality of $\text{K}_2\text{Ni}_2(\text{SeO}_3)_3$. As expected, both the intradimer J_0 and the intraplane J_1 are AFM, but rather surprisingly J_0 is much smaller than J_1 .

The partial densities of states (DOS) of the Ni $3d$, O $2p$, and Se $4p$ orbitals associated with J_0 , J_1 , and J_2 for the AFM-2 state are shown in Figs. 6(b) and 6(c). $\text{K}_2\text{Ni}_2(\text{SeO}_3)_3$ is an insulator with an energy gap of $E_g = 1.1$ and 3.6 eV for $U_{\text{eff}} = 0$ and 6 eV, respectively. The intradimer J_0 is associated with three identical Ni-O2-Ni superexchange (SE) paths, in which the Ni $3d$ orbitals are hybridized with two adjacent O $2p$ orbitals. The small value of J_0 is in line with the small bond angle of $85.04(15)^\circ$. The intraplane J_1 occurs via one Ni-O1-Se1-O1-Ni and one Ni-O2-Se2-O2-Ni super-superexchange (SSE) path, while J_2 has only one Ni-O2-Se2-O2-Ni path [Fig. 2(c)]. It was reported in some quantum magnets that the SSE involving the $(\text{SeO}_3)^{2-}$ group can be very large [43]. There is significant hybridization between the Se $4p$ orbital and the two adjacent O $2p$ orbitals. In the triangular layers, J_2 is negligible compared with J_1 because d_2 is larger than d_1 [Fig. 2(d)] and there is only one SSE path for J_2 [Fig. 2(c)]. It is clear that, although $\text{K}_2\text{Ni}_2(\text{SeO}_3)_3$ has a dimer structure, it exhibits typical triangular-lattice magnetic behavior due to the large AFM exchange via the SSE paths within the triangular plane.

Let us have a discussion on the exchange parameters. The J_0 and J_3 are AFM, which seems to conflict with the interlayer FM exchange required for a net moment ΔM along the c axis. First, the magnitudes of J_0 and J_3 are small; especially when $|J_3| \sim 0$, it is not safe to say that J_3 must be AFM rather than weak FM. Second, the presence of small FM coupling might arise from some yet unknown interlayer exchanges as proposed in $\text{Ba}_2\text{La}_2\text{NiTe}_2\text{O}_{12}$, in which the interlayer exchange obtained from DFT is also tiny and AFM [33], but the neutron diffraction evidenced that triangular layers are ferromagnetically stacked along the c axis. To check the weak interlayer FM coupling in $\text{K}_2\text{Ni}_2(\text{SeO}_3)_3$, a neutron diffraction experiment is desired in the future. Furthermore, it is difficult to simulate the $M(H)$ curve with the calculated exchange

parameters because (i) only a sign of a $1/3$ -like magnetization plateau is observed, the magnetization is not saturated, and there is no information on H_s and M_s and (ii) $\text{K}_2\text{Ni}_2(\text{SeO}_3)_3$ contains triangular-dimer structure and both intradimer J_0 and the intraplane J_1 need to be taken into account. The sign of a $1/3$ -like magnetization plateau in $\text{K}_2\text{Ni}_2(\text{SeO}_3)_3$ is expected to arouse theoretical investigations on the triangular-dimer-lattice antiferromagnet.

Finally, we compare $\text{K}_2\text{Ni}_2(\text{SeO}_3)_3$ with the isostructural $\text{K}_2\text{Co}_2(\text{SeO}_3)_3$ [29]. In $\text{K}_2\text{Co}_2(\text{SeO}_3)_3$, the Co-Co distances are $d_0 = 2.94$ Å and $d_1 = 5.47$ Å, showing no dramatic differences from $\text{K}_2\text{Ni}_2(\text{SeO}_3)_3$. Both compounds exhibit strong geometric frustration and easy-axis anisotropy. In $\text{K}_2\text{Co}_2(\text{SeO}_3)_3$ ($S_{\text{eff}} = 1/2$), no long-range magnetic order was observed down to 0.35 K due to geometric frustration and strong quantum fluctuations. The Curie-Weiss temperature is positive ($\theta_{\text{CW}} = 17.1$ K) for $H \parallel c$, but is largely negative ($\theta_{\text{CW}} = -143.2$ K) for $H \parallel ab$, showing large magnetic anisotropy. The $\chi(T)$ curve along the c axis exhibits a broad hump near 5 K, reflecting the feature of the Co dimer with a spin gap. The $C_p(T)$ curves at zero field and 5 T are composed of a broad peak around 5 K. A well-defined magnetization plateau was observed in the $M(H)$ curve for $H \parallel c$, which is not expected for an $S = 1/2$ dimer antiferromagnet. It is unclear whether this is a $1/3$ magnetization plateau because magnetic saturation is not reached. Hence $\text{K}_2\text{Co}_2(\text{SeO}_3)_3$ possesses characteristics of both spin dimer and TLAF as well as some other unrevealed features, different from the title compound $\text{K}_2\text{Ni}_2(\text{SeO}_3)_3$ exhibiting magnetic behavior of TLAF.

IV. CONCLUSIONS

In summary, we have synthesized the single crystal of the $S = 1$ triangular-dimer-lattice antiferromagnet $\text{K}_2\text{Ni}_2(\text{SeO}_3)_3$, in which the perpendicular-to-plane Ni_2O_9 dimers form a triangular lattice. The main experimental results are (i) a sharp upturn of magnetic susceptibility is observed below $T_N = 5.8$ K, (ii) a single or two magnetic

field-dependent AFM transitions at T_{N1} and T_{N2} are revealed in the heat specific curve, and (iii) a sign of a $1/3$ -like magnetization plateau in the high-field magnetization curve at 2 K is observed. These observations bear a strong resemblance to the magnetic properties of TLAf rather than the $S = 1$ dimer antiferromagnet. The DFT calculations demonstrate that the intradimer exchange ($J_0/k_B = -2.11$ K) is much smaller than the intraplane interdimer exchange ($J_1/k_B = -13.27$ K), although the intradimer distance [$d_0 = 2.9116(18)$ Å] is much smaller than the interdimer distances [$d_1 = 5.4506(3)$ Å and $d_2 = 6.1795(9)$ Å]. The two Ni-O-Se-O-Ni

super-superechange paths are responsible for the dominant J_1 . Magnetically, $K_2Ni_2(SeO_3)_3$ is a TLAf with small easy-axis anisotropy, different from the isostructural $S_{\text{eff}} = 1/2$ Co compound $K_2Co_2(SeO_3)_3$.

ACKNOWLEDGMENTS

This work was supported by the National Natural Science Foundation of China (Grants No. U20A2073 and No. 11874023).

- [1] C. Broholm, R. J. Cava, S. A. Kivelson, D. G. Nocera, M. R. Norman, and T. Senthil, Quantum spin liquids, *Science* **367**, eaay0668 (2020).
- [2] Y. S. Li, P. Gegenwart, and A. A. Tsirlin, Spin liquids in geometrically perfect triangular antiferromagnets, *J. Phys.: Condens. Matter* **32**, 224004 (2020).
- [3] Ch. Rüegg, N. Cavadini, A. Furrer, H.-U. Güdel, K. Krämer, H. Mutka, A. Wildes, K. Habicht, and P. Vorderwisch, Bose-Einstein condensation of the triplet states in the magnetic insulator $TiCuCl_3$, *Nature (London)* **423**, 62 (2003).
- [4] S. E. Sebastian, N. Harrison, C. D. Batista, L. Balicas, M. Jaime, P. A. Sharma, N. Kawashima, and I. R. Fisher, Magnetic-field-induced condensation of triplons in Han Purple pigment $BaCuSi_2O_6$, *Nature (London)* **441**, 617 (2006).
- [5] P. Merchant, B. Normand, K. W. Krämer, M. Boehm, D. F. McMorrow, and Ch. Rüegg, Quantum and classical criticality in a dimerised quantum antiferromagnet, *Nat. Phys.* **10**, 373 (2014).
- [6] M. Vojta, Frustration and quantum criticality, *Rep. Prog. Phys.* **81**, 064501 (2018).
- [7] V. Zapf, M. Jaime, and C. D. Batista, Bose-Einstein condensation in quantum magnets, *Rev. Mod. Phys.* **86**, 563 (2014); Erratum: Bose-Einstein condensation in quantum magnets [Rev. Mod. Phys. **86**, 563 (2014)] **86**, 1453(E) (2014).
- [8] A. N. Vasil'ev, M. M. Markina, and E. A. Popova, Spin gap in low-dimensional magnets, *Low Temp. Phys.* **31**, 203 (2005).
- [9] X.-G. Zhou, Y. Yao, Y. H. Matsuda, A. Ikeda, A. Matsuo, K. Kindo, and H. Tanaka, Particle-hole symmetry breaking in a spin-dimer system $TiCuCl_3$ observed at 100 T, *Phys. Rev. Lett.* **125**, 267207 (2020).
- [10] K. Kodama, M. Takigawa, M. Horvatić, C. Berthier, H. Kageyama, Y. Ueda, S. Miyahara, F. Becca, and F. Mila, Magnetic superstructure in the two-dimensional quantum antiferromagnet $SrCu_2(BO_3)_2$, *Science* **298**, 395 (2002).
- [11] M. Takigawa, M. Horvatic, T. Waki, S. Kramer, C. Berthier, F. Levy-Bertrand, I. Sheikin, H. Kageyama, Y. Ueda, and F. Mila, Incomplete devil's staircase in the magnetization curve of $SrCu_2(BO_3)_2$, *Phys. Rev. Lett.* **110**, 067210 (2013).
- [12] Y. Q. Qin, B. Normand, A. W. Sandvik, and Z. Y. Meng, Multiplicative logarithmic corrections to quantum criticality in three-dimensional dimerized antiferromagnets, *Phys. Rev. Lett.* **118**, 147207 (2017).
- [13] X. C. Liu, Z. W. Ouyang, T. T. Xiao, J. J. Cao, Z. X. Wang, Z. C. Xia, Z. Z. He, and W. Tong, Magnetism and ESR of the $S_{\text{eff}} = 1/2$ antiferromagnet $BaCo_2(SeO_3)_3 \cdot 3H_2O$ with dimer-chain structure, *Phys. Rev. B* **105**, 134417 (2022).
- [14] A. Oosawa, T. Takamasu, K. Tatani, H. Abe, N. Tsujii, O. Suzuki, H. Tanaka, G. Kido, and K. Kindo, Field-induced magnetic ordering in the quantum spin system $KCuCl_3$, *Phys. Rev. B* **66**, 104405 (2002).
- [15] K. Goto, T. Osakabe, K. Kakurai, Y. Uwatoko, A. Oosawa, J. Kawakami, and H. Tanaka, Softening of magnetic excitations leading to pressure-induced quantum phase transition in gapped spin system $KCuCl_3$, *J. Phys. Soc. Jpn.* **76**, 053704 (2007).
- [16] Ch. Rüegg, M. Oetli, J. Schefer, O. Zaharko, A. Furrer, H. Tanaka, K. W. Kramer, H.-U. Güdel, P. Vorderwisch, K. Habicht, T. Polinski, and M. Meissner, Neutron scattering study of the field-dependent ground state and the spin dynamics in spin-one-half NH_4CuCl_3 , *Phys. Rev. Lett.* **93**, 037207 (2004).
- [17] S. Allenspach, P. Puphal, J. Link, I. Heinmaa, E. Pomjakushina, C. Krellner, J. Lass, G. S. Tucker, C. Niedermayer, S. Imajo, Y. Kohama, K. Kindo, S. Kramer, M. Horvatic, M. Jaime, A. Madsen, A. Mira, N. Laflorencie, F. Mila, B. Normand *et al.*, Revealing three-dimensional quantum criticality by Sr substitution in Han purple, *Phys. Rev. Res.* **3**, 023177 (2021).
- [18] Y. H. Matsuda, N. Abe, S. Takeyama, H. Kageyama, P. Corboz, A. Honecker, S. R. Manmana, G. R. Foltin, K. P. Schmidt, and F. Mila, Magnetization of $SrCu_2(BO_3)_2$ in ultrahigh magnetic fields up to 118 T, *Phys. Rev. Lett.* **111**, 137204 (2013).
- [19] T. Ziman, J. P. Boucher, Y. Inagaki, and Y. Ajiro, Field-induced magnetic order of $Cs_3Cr_2Br_9$ and $Cs_3Cr_2Cl_9$, *J. Phys. Soc. Jpn.* **74**, 119 (2005).
- [20] D. Brüning, T. Frohlich, D. Gorkov, I. Cisarova, Y. Skourski, L. Rossi, B. Bryant, S. Wiedmann, M. Meven, A. Ushakov, S. V. Streltsov, D. Khomskii, P. Becker, L. Bohaty, M. Braden, and T. Lorenz, Multiple field-induced phases in the frustrated triangular magnet $Cs_3Fe_2Br_9$, *Phys. Rev. B* **104**, 064418 (2021).
- [21] H.-J. Koo, K.-S. Lee, and M.-H. Whangbo, Spin dimer analysis of the magnetic structures of $Ba_3Cr_2O_8$, $Ba_3Mn_2O_8$, Na_4FeO_4 , and Ba_2CoO_4 with a three-dimensional network of isolated MO_4 ($M = Cr, Mn, Fe, Co$) tetrahedra, *Inorg. Chem.* **45**, 10743 (2006).
- [22] Y. Singh and D. C. Johnston, Singlet ground state in the spin-1/2 dimer compound $Sr_3Cr_2O_8$, *Phys. Rev. B* **76**, 012407 (2007).
- [23] A. A. Aczel, Y. Kohama, C. Marcenat, F. Weickert, M. Jaime, O. E. Ayala-Valenzuela, R. D. McDonald, S. D. Selesnic, H. A. Dabkowska, and G. M. Luke, Field-induced Bose-Einstein condensation of triplons up to 8 K in $Sr_3Cr_2O_8$, *Phys. Rev. Lett.* **103**, 207203 (2009).

- [24] E. C. Samulon, Y. Kohama, R. D. McDonald, M. C. Shapiro, K. A. Al-Hassanieh, C. D. Batista, M. Jaime, and I. R. Fisher, Asymmetric quintuplet condensation in the frustrated $S = 1/4$ 1 spin dimer compound $\text{Ba}_3\text{Mn}_2\text{O}_8$, *Phys. Rev. Lett.* **103**, 047202 (2009).
- [25] M. B. Stone, M. D. Lumsden, V. O. Garlea, B. Grenier, E. Ressouche, E. C. Samulon, and I. R. Fisher, Field induced spin density wave and spiral phases in a layered antiferromagnet, *Phys. Rev. B* **92**, 020415(R) (2015).
- [26] A. Gazizulina, D. L. Quintero-Castro, D. Wulferding, J. Teyssier, K. Prokes, F. Yokaichiya, and A. Schilling, Tuning the orbital-lattice fluctuations in the mixed spin-dimer system $\text{Ba}_{3-x}\text{Sr}_x\text{Cr}_2\text{O}_8$, *Phys. Rev. B* **98**, 144115 (2018).
- [27] Z. Wang, D. L. Quintero-Castro, S. Zherlitsyn, S. Yasin, Y. Skourski, A. T. M. N. Islam, B. Lake, J. Deisenhofer, and A. Loidl, Field-induced magnonic liquid in the 3D spin-dimerized antiferromagnet $\text{Sr}_3\text{Cr}_2\text{O}_8$, *Phys. Rev. Lett.* **116**, 147201 (2016).
- [28] M. Wildner, Structure of $\text{K}_2\text{Co}_2(\text{SeO}_3)_3$, *Acta Crystallogr.* **C50**, 336 (1994).
- [29] R. Zhong, S. Guo, L. T. Nguyen, and R. J. Cava, Frustrated spin-1/2 dimer compound $\text{K}_2\text{Co}_2(\text{SeO}_3)_3$ with easy-axis anisotropy, *Phys. Rev. B* **102**, 224430 (2020).
- [30] G. M. Sheldrick, Crystal structure refinement with *SHELXL*, *Acta Crystallogr., C: Struct. Chem.* **71**, 3 (2015).
- [31] J. P. Perdew, K. Burke, and M. Ernzerhof, Generalized gradient approximation made simple, *Phys. Rev. Lett.* **77**, 3865 (1996).
- [32] P. Blaha, K. Schwarz, F. Tran, R. Laskowski, G. K. H. Madsen, and L. D. Marks, WIEN2k: An APW+lo program for calculating the properties of solids, *J. Chem. Phys.* **152**, 074101 (2020).
- [33] M. Saito, M. Watanabe, N. Kurita, A. Matsuo, K. Kindo, M. Avdeev, H. O. Jeschke, and H. Tanaka, Successive phase transitions and magnetization plateau in the spin-1 triangular-lattice antiferromagnet $\text{Ba}_2\text{La}_2\text{NiTe}_2\text{O}_{12}$ with small easy-axis anisotropy, *Phys. Rev. B* **100**, 064417 (2019).
- [34] S. Miyashita and H. Kawamura, Phase transitions of anisotropic heisenberg antiferromagnets on the triangular lattice, *J. Phys. Soc. Jpn.* **54**, 3385 (1985); F. Matsubara, Magnetic ordering in a hexagonal antiferromagnet, *ibid.* **51**, 2424 (1982).
- [35] R. Zhong, S. Guo, and R. J. Cava, Frustrated magnetism in the layered triangular lattice materials $\text{K}_2\text{Co}(\text{SeO}_3)_2$ and $\text{Rb}_2\text{Co}(\text{SeO}_3)_2$, *Phys. Rev. Mater.* **4**, 084406 (2020).
- [36] Z. Lu, L. Ge, G. Wang, M. Russina, G. Gunther, C. R. dela Cruz, R. Sinclair, H. D. Zhou, and J. Ma, Lattice distortion effects on the frustrated spin-1 triangular- antiferromagnet $\text{A}_3\text{NiNb}_2\text{O}_9$ ($A = \text{Ba}, \text{Sr}$ and Ca), *Phys. Rev. B* **98**, 094412 (2018).
- [37] M. Lee, E. S. Choi, J. Ma, R. Sinclair, C. R. Dela Cruz, and H. D. Zhou, Magnetism and multiferroicity of an isosceles triangular lattice antiferromagnet $\text{Sr}_3\text{NiNb}_2\text{O}_9$, *J. Phys.: Condens. Matter* **28**, 476004 (2016).
- [38] M. Lee, J. Hwang, E. S. Choi, J. Ma, C. R. Dela Cruz, M. Zhu, X. Ke, Z. L. Dun, and H. D. Zhou, Series of phase transitions and multiferroicity in the quasi-two-dimensional spin-1/2 triangular-lattice antiferromagnet $\text{Ba}_3\text{CoNb}_2\text{O}_9$, *Phys. Rev. B* **89**, 104420 (2014).
- [39] K. M. Ranjith, K. Brinda, U. Arjun, N. G. Hegde, and R. Nath, Double phase transition in the triangular antiferromagnet $\text{Ba}_3\text{CoTa}_2\text{O}_9$, *J. Phys.: Condens. Matter* **29**, 115804 (2017).
- [40] J. Hwang, E. S. Choi, F. Ye, C. R. Dela Cruz, Y. Xin, H. D. Zhou, and P. Schlottmann, Successive magnetic phase transitions and multiferroicity in the spin-one triangular-lattice antiferromagnet $\text{Ba}_3\text{NiNb}_2\text{O}_9$, *Phys. Rev. Lett.* **109**, 257205 (2012).
- [41] M. Liu, H. M. Zhang, X. Huang, C. Y. Ma, S. Dong, and J. M. Liu, Two-step antiferromagnetic transitions and ferroelectricity in spin-1 triangular-lattice antiferromagnetic $\text{Sr}_3\text{NiTa}_2\text{O}_9$, *Inorg. Chem.* **55**, 2709 (2016).
- [42] I. P. Muthuselvam, R. Sankar, A. V. Ushakov, G. N. Rao, S. V. Streltsov, and F. C. Chou, Two-step antiferromagnetic transition and moderate triangular frustration in $\text{Li}_2\text{Co}(\text{WO}_4)_2$, *Phys. Rev. B* **90**, 174430 (2014).
- [43] Z. Wang, M. Schmidt, Y. Goncharov, V. Tsurkan, H.-A. Krug von Nidda, A. Loidl, and J. Deisenhofer, Terahertz spectroscopy in the pseudo-Kagome system $\text{Cu}_3\text{Bi}(\text{SeO}_3)_2\text{O}_2\text{Br}$, *Phys. Rev. B* **86**, 174411 (2012).